



Article

A Noise De-Correlation Based Sun Glint Correction Method and Its Effect on Shallow Bathymetry Inversion

Aijun Cui ¹, Jingyu Zhang ^{2,3,*} , Yi Ma ^{2,3} and Xi Zhang ⁴¹ College of Geodesy and Geomatics, Shandong University of Science and Technology, Qingdao 266590, China² Lab of Marine Physics and Remote Sensing, First Institute of Oceanography, Ministry of Natural Resources, Qingdao 266061, China³ Technology Innovation Center for Ocean Telemetry, Ministry of Natural Resources, Qingdao 266061, China⁴ National Satellite Ocean Application Service, Beijing 100089, China

* Correspondence: zhangjingyu@fio.org.cn; Tel.: +86-88967870

Abstract: Sun glint on the sea surface is the unavoidable noise in optical remote sensing images. Water depth retrieval based on optical remote sensing images is vulnerable to sun glint contamination. Different sun glint correction methods and their possible effects on improving the accuracy of optical remote sensing water depth inversion are worth adequately discussing. Considering the problem that traditional sun glint correction methods are not well applied in shallow or turbid water areas, this paper proposes a sun glint correction method based on noise de-correlation (ND-SGC) which is not affected by the essential characteristics of the water body itself and does not require any auxiliary data. In this paper, we analyze the spectral fidelity of remote sensing images by using ND-SGC method and traditional methods for sun glint correction, and compare the accuracy of bathymetry inversion in different water depth cases and between sun glint pixels and sun glint-free pixels. The experimental results indicated that: (1) the ND-SGC method gives different penalty weights to sun glint pixels and sun glint-free pixels, which meaningfully improves the bathymetric inversion accuracy of sun glint pixels and maintains the bathymetric inversion accuracy of sun glint-free pixels, and is applicable to any water depth range; (2) the ND-SGC method improves bathymetric inversion accuracy in the extremely shallow water region (0–2 m) and shallow water region (2–11 m), while the conventional method suppresses bathymetric inversion accuracy in these two water depth ranges; (3) the ND-SGC method maintains the inversion accuracy of the sun glint-free pixels, while the traditional Hedley method and Goodman method increase the mean relative error (MRE) of these pixels by a maximum of 6.7% and 8.8%, respectively; (4) the ND-SGC method preserves the inherent spectral information of the remote sensing image well, while the spectral fidelity index of the images corrected by traditional methods shows a certain degree of distortion of the image's spectrum.

Keywords: sun glint correction; optical remote sensing; bathymetry; noise de-correlation; various water depth ranges



Citation: Cui, A.; Zhang, J.; Ma, Y.; Zhang, X. A Noise De-Correlation Based Sun Glint Correction Method and Its Effect on Shallow Bathymetry Inversion. *Remote Sens.* **2022**, *14*, 5981. <https://doi.org/10.3390/rs14235981>

Academic Editors:
Guillaume Ramillien and
Andrzej Staczyn

Received: 20 September 2022

Accepted: 23 November 2022

Published: 25 November 2022

Publisher's Note: MDPI stays neutral with regard to jurisdictional claims in published maps and institutional affiliations.



Copyright: © 2022 by the authors. Licensee MDPI, Basel, Switzerland. This article is an open access article distributed under the terms and conditions of the Creative Commons Attribution (CC BY) license (<https://creativecommons.org/licenses/by/4.0/>).

1. Introduction

Water depth remains a fundamental parameter of the marine environment. With abundant data sources and high resolution, satellite optical remote sensing has naturally become a vital means of properly obtaining bathymetric data over large areas at the time of measurement [1–8]. The signals received by the optical remote sensors contain sunlight information reflected by the seabed, which constitutes the physical basis for the shallow water depth inversion with optical remote sensing. In other words, the information reflected from the seabed into the optical remote sensor is the direct reflection of the underwater topography, i.e., the source of information for optical remote sensing in water depths [9]. However, due to the optical remote sensor observation geometry and the sea surface wave slope, the solar rays are directly reflected by the sea surface into the remote sensor, forming

sun glint on some image pixels [10,11]. Sun glint, to some extent, interferes with the submarine light reflection information in the corresponding region, which seriously affects the accuracy of the bathymetric inversion [12,13]. Therefore, sun glint correction is an essential image pre-processing task for optical remote sensing inversion of water depth.

The sun glint correction methods routinely used in remote sensing images are divided into methods based on sea surface properties and methods based on inter-band relationships. The sea surface property-based methods typically consider sun glint to be related to sea surface roughness. The slope of the sea surface is obtained from the wind field data to obtain the glint components [14–16]. This method is barely implemented because wind field data is sometimes difficult to obtain or the resolution is far from that of remote sensing images. After radiometric and atmospheric correction, the reflectance of the near infrared (NIR) band in the clean deep-water region should be zero but usually is not, which is generally caused by sun glint. The principle of the sun glint correction methods based on the inter-band relationship is the strong absorption of water in the NIR band. The sun glint components are removed according to the physical relationship between the NIR and other bands [17–20]. Such methods are simple to operate, effective and most widely used. However, the NIR band is generally not zero in extremely shallow water or unclean water, which will affect the sun glint correction effect.

Scholars have introduced a total variation (TV) based method to image processing. This method was initially utilized for blurred image recovery and background noise removal. Liu et al. [21] proposed a regularization model based on structural gradient and texture de-correlation, assigning different weights to different pixels, solving the problem of equal glint removal effort on signal pixels and noise pixels and applying the model to the extraction of target information from images. In recent years, this type of method is additionally used for remote sensing image sun glint correction, which considers that the sun glint-contaminated optical remote sensing image is a combination of the sun glint component image and the original sun glint-free image, and if the correlation between these two components is minimized, a sun glint-free remote sensing image can be obtained [22,23]. Duan et al. [24] applied a method based on texture-aware total variation for sun glint correction before oil spill classification in hyperspectral images, so that the weight of sun glint image pixels is larger than that of sun glint-free image pixels, thus effectively removing the sun glint component of sun glint image pixels.

For bathymetric inversion, the inversion result is easily affected by the complex environment of near-shore water bodies. At the same time, the remote sensing images cover a large area, with high resolution of image pixels and a large amount of data, and the image processing calculation can easily fall into local paralysis. Considering the problems that traditional sun glint correction methods are difficult to be applied in areas lacking auxiliary data or near-shore water environment, and the complex calculation of texture-aware total variation algorithm can easily fall into local paralysis, this paper proposes a noise de-correlation-based sun glint correction method, which does not need auxiliary data support and has no requirement on water environment, and is applicable to the sun glint correction of remote sensing images of water bodies in areas lacking auxiliary data. The ND-SGC method and two traditional sun glint correction methods have been used to analyze the spectral fidelity of the correction results. Using Sentinel-2 and WorldView-2 remote sensing images, the most representative Log-Linear model and Stumpf model in bathymetric inversion were used for bathymetric inversion to investigate the effect of different sun glint correction models for different bathymetric ranges, and to analyze the effect of sun glint correction on the accuracy of bathymetric inversion of sun glint pixels and sun glint-free pixels.

2. Materials and Methods

2.1. The Study Areas and Data Sets

This paper takes the Dongdao Island, the east reef plate of Tiexian Jiao and Taiping Island in the South China Sea as the study areas. Dongdao Island is located between

16°39′–16°41′N and 112°43′–112°45′E. It belongs to Sansha City, Hainan Province, China. The island has an area of about 1.7 km² and is roughly rectangular in shape, with a length of about 2400 m and a width of about 1 km. Tiexian Jiao is one of the islands and reefs in the Spratly Islands of China, located in the range of 11°1′–11°4′N and 114°11′–114°16′E. It is the general name of the coral reef at the northern edge of the western atoll of Zhongye Group Reef. This area is adjacent to the west of Zhongye Group Reef. Tiexian Jiao runs northeast-southwest. The east reef plate of the Tiexian Jiao is utilized as the study area. It is located 4.5 km northwest of Zhongye Island and is a circular reef disk with a diameter of about 930 m and an area of 0.86 km² with sandbar development. Taiping Island, located in the northwest corner of Zhenghe Group Reef in the northern part of Spratly Islands in the South China Sea, is located at 10°22′38″N and 114°21′59″E, with an area of 0.43 km², 1289 m east to west and 366 m north to south. The above three areas are far away from the continent, less affected by human activities, so the water in those areas is clear. They are ideal areas for bathymetric inversion.

The optical satellite image of Taiping Island area and Tiexian Jiao came from WorldView-2 with a resolution of 2 m; both images were acquired on 23 May 2022. Dongdao Island's satellite image came from Sentinel-2 with a resolution of 10 m, and was acquired on 13 February 2021. Sun glint contamination is evident in all three images, shown in Figure 1. Details about the basic attributes of remote sensing images are shown in Table 1.

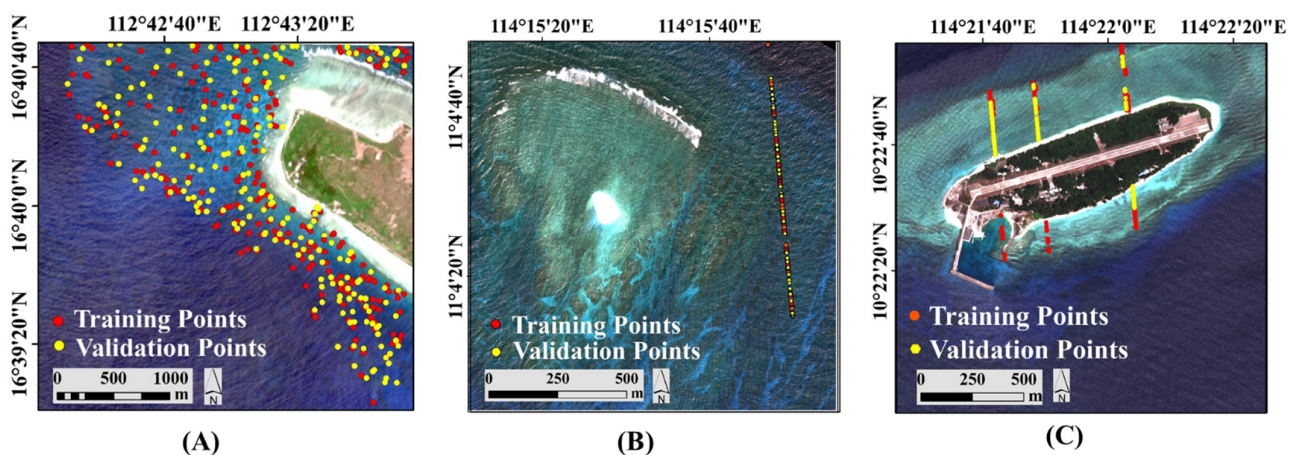


Figure 1. The satellite images of study areas and the distribution of actual water depth points. (A) Dongdao Island; (B) Tiexian Jiao; (C) Taiping Island.

Table 1. Basic attributes of remote sensing images.

Area	Satellite Image	Actual Water Depth Data Type	Resolution (m)	Spatial Domain (pixel)	Acquisition Time
Dongdao Island	Sentinel-2	Single-beam	10	328 × 328	13 February 2021
Tiexian Jiao	WorldView-2	ICESat-2	2	668 × 668	23 May 2022
Taiping Island	WorldView-2	ICESat-2	2	896 × 896	23 May 2022

The actual water depth data of the Taiping Island and Tiexian Jiao came from ICESat-2 [25,26], and both images were acquired in 2022. The actual water depth data of Dongdao Island were obtained by a single beam echosounder in 2011. The number of actual water depth points in the three study areas is shown in Table 2. In this paper, water depth points are selected in different water depth ranges and on both sun glint image pixels and sun glint-free image pixels.

Table 2. The number of water depth training points and validation points.

Area	Overall Training Points	Overall Validation Points	With Sun Glint: Training Points	With Sun Glint: Validation Points	Without Sun Glint: Training Points	Without Sun Glint: Validation Points
Dongdao Island	215	190	114	93	101	97
Tiexian Jiao	85	80	34	31	51	49
Taiping Island	789	612	591	333	198	279

2.2. Data Processing

Data processing includes remote sensing image processing and water depth data processing. Radiometric calibration and atmospheric correction of remote sensing images are required before sun glint correction. Radiometric calibration converts DN value into radiance value with practical physical meaning. The conversion formula for WorldView-2 images is as follows:

$$L(\lambda_i) = \frac{absCalFactor_i \times DN_i}{\Delta\lambda_i}, \quad (1)$$

where $L(\lambda_i)$ is the radiance value of band i ; $absCalFactor_i$ is the absolute scaling factor; DN_i is the gray value of image pixel; and $\Delta\lambda_i$ is the equivalent band width.

Atmospheric correction eliminates atmospheric effects to obtain a more realistic ground level radiation or reflectance. The frequently used FLAASH model utilizes the MODTRAN4+ model to correct the image after radiometric calibration with the following equation:

$$L^* = \frac{A\rho}{1 - \rho_e S} + \frac{B\rho_e}{1 - \rho_e S} + L_a^*, \quad (2)$$

where L^* is the total reflectance received by the sensor; A and B are calculation coefficients; ρ is the surface reflectance; ρ_e is the average surface reflectance of the image pixels and the surrounding environment; L_a^* is atmospheric backscatter coefficient; S is the atmospheric hemispheric reflectance.

Sentinel-2A's L2A data are bottom-of-atmosphere reflectance data after radiometric calibration and atmospheric correction. The L2A data do not require additional radiometric calibration and atmospheric correction, although the number of images at this level is low. Sentinel-2A L1C data are atmospheric apparent reflectance products after orthorectification correction and geometric refinement at the sub-image level. L1C data can be atmospherically corrected using the sen2cor plug-in available from the European Space Agency's website.

The water depth obtained by remote sensing image inversion is the instantaneous water depth at the time of remote sensing image imaging. The time difference between in-situ bathymetry data acquisition and remote sensing image imaging time will cause large errors. Tidal correction is to add the measured water depth to the tidal height at a certain time to determine the instantaneous water depth at that time, eliminating the error caused by the difference in time. According to the tide table, the tide height at the time of image acquisition was 0.75 m for Dongdao Island, 0.51 m for Taiping Island, and 0.33 m for Tiexian Jiao.

2.3. Sun Glint Correction Models

2.3.1. A Noise De-Correlation Based Sun Glint Correction Method

The optical remote sensing image $O_{m \times m}$ with sun glint contamination can be considered as the combination of sun glint noise component image $S_{m \times m}$ and glint-free image $X_{m \times m}$, i.e., $O = X + S$, where m is the spatial dimensions. In order to obtain the sun glint-free images, X needs to be extracted from O mixed with the sun glint noise component, i.e., to achieve maximum de-correlation between X and S . The image component decor-

relation problem usually has no unique solution. Considering that the sun glint region possesses higher reflectance values than the surrounding sun glint-free area, the standard total variation regularization method [27–30] can provide a priori knowledge for this image decomposition problem to achieve the maximum de-correlation of X and S . The variation of X at pixel i is represented as $\|D_i X\|_2$, where $D_i X$ is the first-order difference of X at pixel i in both horizontal and vertical directions, i.e., a difference matrix [27]. The total variation of all pixels of the image is expressed as $TV(X) = \sum_{i=1}^{m^2} \|D_i X\|_2$.

The total variation obtained by adding the sun glint information to the standard total variation can better distinguish between the sun glint areas and the sun glint-free areas. The objective formula of the regularization model to achieve the minimization of total variation with the addition of sun glint information is as follows:

$$x = \underset{x}{\operatorname{argmin}} \left\{ \frac{\mu}{2} \|O - X\|_F^2 + \eta \sum_{i=1}^{m \times m} \|D_i X\|_2 + \sum_{i=1}^{m \times m} |O_i - X_i| \cdot \|D_i X\|_2 \right\}, \quad (3)$$

μ, η in Equation (3) are weighting factors. The recommended settings are $\mu = 2$, $\eta = 0.015$ [21,24] and $\sum_{i=1}^{m \times m} |O_i - X_i| \cdot \|D_i X\|_2$ increases the degree of distinction between sun glint and sun glint-free areas.

The above regularization model is optimized using the Augmented Lagrangian method. The Augmented Lagrangian method is used to solve optimization problems under equation constraints by decomposing a problem into multiple sub-problems and adding constraints. Firstly, introduce auxiliary variables Y, A :

$$Y_i = D_i X, i = 1, 2, \dots, m^2, \quad (4)$$

$$A = O - X, \quad (5)$$

Then, Equation (3) is divided into three sub-problems of optimization of X, Y, A . In addition, we add penalty factors β_1, β_2 , multipliers $\lambda_j = [\lambda_{j1}, \lambda_{j2}, \dots, \lambda_{jm^2}]$, $j = 1, 2$. Empirically, we set $\beta_1 = 5, \beta_2 = 20$. Thus, the augmented Lagrangian formula becomes as follows:

$$L(X, Y, S, \lambda) = \underset{X, Y, A}{\operatorname{argmin}} \left\{ \frac{\mu}{2} \|A\|_F^2 + \sum_{i=1}^{m^2} (\eta + |A_i|) \cdot \|Y_i\|_2 - \lambda_1^T (Y - D) - \lambda_2^T (A - X + O) + \frac{\beta_1}{2} \sum_{i=1}^{m^2} \|Y_i - D_i X\|_2^2 + \frac{\beta_2}{2} \|A - X + O\|_F^2 \right\}, \quad (6)$$

The optimization equations for the three sub-problems are as follows:

By fixing X and A variable, the optimal Y variable in (6) can be obtained:

$$Y^{k+1} = \underset{Y}{\operatorname{argmin}} \left\{ \sum_{i=1}^{m^2} (\eta + |A_i^k|) \cdot \|Y_i\|_2 + \frac{\beta_1}{2} \sum_{i=1}^{m^2} \|Y_i - D_i X^k - \frac{\lambda_1^k}{\beta_1}\|_2^2 \right\}, \quad (7)$$

By fixing X and Y variables, the optimal A variable in (6) can be obtained:

$$A^{k+1} = \underset{A}{\operatorname{argmin}} \left\{ \sum_{i=1}^{m^2} (\eta + |A_i|) \cdot \|Y_i^{k+1}\|_2 + \frac{\mu + \beta_2}{2} \|A - X^k + O - \frac{\lambda_2^k}{\beta_2}\|_F^2 \right\}, \quad (8)$$

By fixing A and Y variables, the optimal X variable in (6) can be obtained:

$$X^{k+1} = \underset{X}{\operatorname{argmin}} \left\{ \frac{1}{2} \left(\beta_1 \sum_{i=1}^{m^2} \|Y_i^{k+1} - D_i X - \frac{\lambda_1^k}{\beta_1}\|_2^2 + \beta_2 \|A^{k+1} - X + O - \frac{\lambda_2^k}{\beta_2}\|_F^2 \right) \right\}, \quad (9)$$

Let:

$$\frac{\partial}{\partial X} \left(\underset{X}{\operatorname{argmin}} \left\{ \frac{1}{2} \left(\beta_1 \sum_{i=1}^{m^2} \|Y_i^{k+1} - D_i X - \frac{\lambda_1^k}{\beta_1}\|_2^2 + \beta_2 \|A^{k+1} - X + O - \frac{\lambda_2^k}{\beta_2}\|_F^2 \right) \right\} \right) = 0, \quad (10)$$

We can obtain the following:

$$(\beta_1 D^T D + \beta_2) X = \beta_1 D^T \left(Y^{k+1} - \frac{\lambda_1^k}{\beta_1} \right) + \beta_2 \left(A + O - \frac{\lambda_2^k}{\beta_2} \right), \quad (11)$$

Performing k iterations for $X, Y, A, \lambda_1, \lambda_2$ simultaneously to obtain the optimal solution $(X^{k+1}, Y^{k+1}, A^{k+1})$ starting from $\lambda_1^0 = \lambda_2^0 = 0, X_{m \times m} = O_{m \times m}$. It is worth noting that this method can only handle a square matrix.

The iterative formulas are as follows:

$$Y_i^{k+1} = \left(D_i X^k + \lambda_{1i}^k - \eta - \frac{|A_i^k|}{\beta_1} \right) * \left(\frac{(D_i X^k + \frac{\lambda_{1i}^k}{\beta_1})}{\|DX^k + \frac{\lambda_1^k}{\beta_1}\|_2} \right), \quad (12)$$

$$A^{k+1} = \text{sgn} \left\{ \frac{\beta_2}{\mu + \beta_2} \left(X + \frac{\lambda_2}{\beta_2} \right) \right\} \odot \left\{ \frac{\beta_2}{\mu + \beta_2} \left(X - O + \frac{\lambda_2}{\beta_2} - D \right) \right\}, \quad (13)$$

$$X^{k+1} = \mathcal{F}^{-1} \left\{ \frac{\mathcal{F} \{ \beta_1 (DX^k)^T (Y^{k+1} - \frac{\lambda_1^k}{\beta_1}) + \beta_2 (A + O - \frac{\lambda_2^k}{\beta_2}) \}}{\beta_1 + \beta_2} \right\}, \quad (14)$$

$$\lambda_1^{k+1} = \lambda_1^k - \beta_1 (Y^{k+1} - DX^{k+1}), \quad (15)$$

$$\lambda_2^{k+1} = \lambda_2^k - \beta_2 (A^{k+1} - X^{k+1} + O), \quad (16)$$

Sgn represents the symbolic function and the formula is given in (17). \mathcal{F} represents the 2D discrete Fourier transform and \odot represents a point-wise product function.

$$\text{sgn} = \begin{cases} -1, & t < 0 \\ 0, & t = 0 \\ 1, & t > 0 \end{cases}, \quad (17)$$

The flow chart of the algorithm is shown in Figure 2.

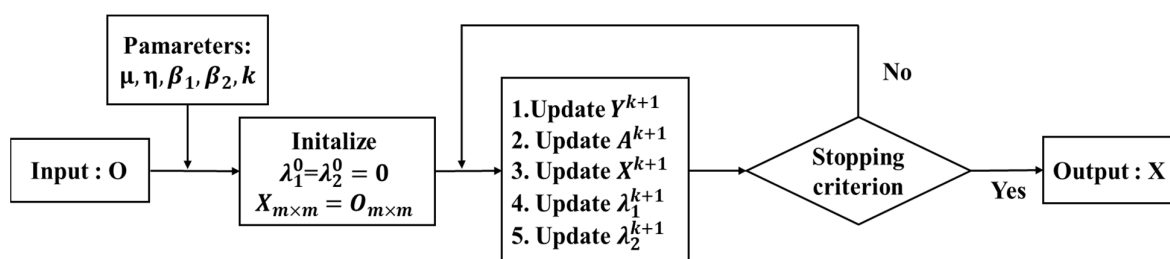


Figure 2. The flow chart of the ND-SGC method.

2.3.2. Other Models

Hedley et al., selected multiple sun glint pixels in the deep-water area as sample points on the image to obtain the key parameters for sun glint correction. The Mathematical analytic equation of this model is as follows:

$$R'_i = R_i - b_i * (R_{NIR} - Min_{NIR}), \quad (18)$$

where R'_i is the corrected reflectance from the visible band i ; R_i is reflectance from visible band i ; b_i is regression slope; R_{NIR} is reflectance from NIR band; Min_{NIR} is minimum value of NIR band.

The covariance function or the least squares method can be used to calculate the slope b_i . The covariance function is calculated as follows:

$$\rho_{ij} = \frac{1}{N} \sum_{n=1}^N R_{in} R_{jn} - \frac{1}{N} \sum_{i=1}^N R_{in} \frac{1}{N} \sum_{j=1}^N R_{jn}, \quad (19)$$

R_{in} , R_{jn} are the n th sample values of visible band i and NIR band respectively. N is the total number of samples. The sun glint correlation coefficient between the visible band i and the NIR band can be given by the following equation:

$$b_i = \frac{\rho_{ij}}{\rho_{jj}}, \quad (20)$$

Goodman et al. corrected each pixel independently for each band and calculated the corrected offset using the 640 nm and 750 nm bands, and the offset was equal for each band:

$$\Delta = A + B * [R_{640} - R_{750}], \quad (21)$$

where Δ indicates the offset parameter, which is calculated from 640 nm and 750 nm bands and two constants A and B . The best valuation of A and B is given by Goodman using experimental test; the recommended value is $A = 0.000019$, $B = 0.1$.

$$R'_i = R_i - R_{750} + \Delta, \quad (22)$$

2.4. Shallow Water Bathymetry Models

2.4.1. Log-Linear Model

According to the characteristics of light radiative transfer in water bodies, Lyzenga et al. proposed a multi-band linear model for water depth inversion of multi-spectral images based on the formerly available models. The formula is as follows:

$$\hat{Z} = \alpha_0 + \sum_{i=1}^N \alpha_i \ln[R_W(\lambda_i) - R_\infty(\lambda_i)], \quad (23)$$

Here, \hat{Z} is the derived bathymetry; α_i ($i = 0, 1, \dots, N$) are the model parameters to be determined; N is the number of spectral bands; $R_W(\lambda_i)$ is remote sensing reflectance (after atmospheric correction) in band i ; $R_\infty(\lambda_i)$ the deep-water remote sensing reflectance. This formulation, known as the Log-Linear model, is the most widely used model for bathymetry inversion from multispectral remote sensing images.

2.4.2. Stumpf Model

The Log-Linear model may cause the situation that the off-water radiance in the deep water region is greater than the radiance received by the sensor, which makes the equation meaningless. To allow the equation to be used in the low albedo region, Stumpf improved it by proposing a logarithmic ratio model. The formula is as follows:

$$\hat{Z} = m_1 * \frac{\ln[nR_W(\lambda_i)]}{\ln[nR_W(\lambda_j)]} + m_0, \quad (24)$$

where m_0 and m_1 are the regression coefficients; n is the band adjustment factor which ensures that the value after taking the logarithm is reasonable and that the logarithm is positive in all cases; $R_W(\lambda_i)$, $R_W(\lambda_j)$ are the remote sensing reflectance (after atmospheric correction) of visible band i and j respectively.

2.4.3. Accuracy Evaluation Methods

The mean relative error (MRE) and mean absolute error (MAE) were used to make a quantitative evaluation of the accuracy of the water depth inversion. The corresponding formulas are as follows:

$$MRE = \frac{\sum_{i=1}^N \frac{|Z_i - X_i|}{Z_i}}{N}, \quad (25)$$

$$MAE = \frac{\sum_{i=1}^N |Z_i - X_i|}{N}, \quad (26)$$

In the above two formula, Z_i is the actual water depth; X_i is the estimated water depth; N is the number of water depth points.

2.5. Spectral Fidelity Assessment Indexes

1. Correlation Coefficient (CC).
2. Error.
3. Spectral Angle Mapper (SAM).

CC refers to the similarity of the grayscale values of image pixels before and after sun glint correction, which reflects the spectral similarity of the two images. Larger values of the spectral correlation coefficient indicate a better spectral fidelity.

$$C = \frac{1}{k} \sum_{i=1}^k \frac{\sum_{i=1}^M \sum_{j=1}^N (F_{(i,j)k} - \overline{F_{(i,j)k}}) (f_{(i,j)k} - \overline{f_{(i,j)k}})}{\sqrt{\sum_{i=1}^M \sum_{j=1}^N (F_{(i,j)k} - \overline{F_{(i,j)k}})^2 \sum_{i=1}^M \sum_{j=1}^N (f_{(i,j)k} - \overline{f_{(i,j)k}})^2}}, \quad (27)$$

where $F_{(i,j)}$ is the image pixel value before sun glint correction; $f_{(i,j)}$ is the corrected image pixel value; $\overline{F_{(i,j)}}$, $\overline{f_{(i,j)}}$ are the average image pixel values of the image before and after sun glint correction, respectively; M and N are the number of rows and columns of the image respectively; K represents the number of bands.

The *Error* can reflect the degree of spectral deviation via sun glint correction. A smaller error value means that the glint-corrected image has less spectral distortion and better spectral fidelity.

$$Error = \frac{1}{M \times N} \sum_{i=1}^M \sum_{j=1}^N \left(\frac{1}{k} \sum_{i=1}^k |F_{(i,j)k} - f_{(i,j)k}| \right), \quad (28)$$

The Spectral Angle Mapper refers to the angle between two spectral vectors in linear space. The closer the value is to 0, the smaller the spectral angle is and the smaller the spectral distortion is.

$$SAM = \frac{1}{k} \sum_{i=1}^k \arccos \left\{ \frac{\sum_{i=1}^{M \times N} (F_{(i,j)k} \times f_{(i,j)k})}{\sqrt{\sum_{i=1}^{M \times N} F_{(i,j)k}^2} \sqrt{\sum_{i=1}^{M \times N} f_{(i,j)k}^2}} \right\}, \quad (29)$$

3. Results

3.1. Comparison of Visual Effect

Figure 3 shows the comparison between the original images and the remote sensing images after the sun glint correction. From a visual perspective, the Hedley method causes the blue information in the RGB composite image of the Dongdao Island region to be too prominent, while the Goodman method makes the green information in the composite image too prominent. These two methods cause one or more bands to be highlighted after band stacking. In Taiping Island area, Hedley's method and Goodman's method make optical satellite images show obvious visual distortion. This may be due to the fact that the water depth in the Taiping Island area is too shallow and the NIR band is not fully absorbed by the water, making the sun glint correction results of the two models poorer.

This may cause drastic changes in the spectra of optical satellite images, which will have a very negative impact on the bathymetric inversion. In addition, sun glint noise is usually attached to waves. Sun glint noise should be removed while preserving the wave shape. Otherwise, spectral distortion will occur and the accuracy of water depth inversion will be affected.

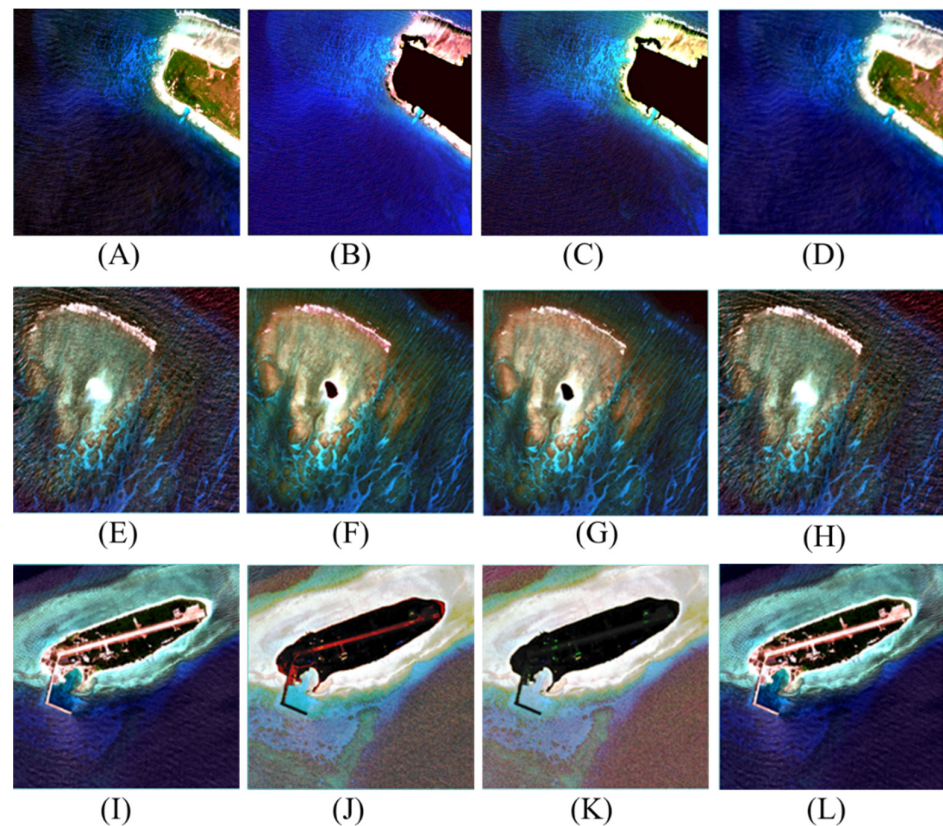


Figure 3. Satellite images before and after sun glint correction. (A–D) are the original image of Dongdao Island, the Hedley method, the Goodman method, and the ND-SGC method, respectively. (E–H) are the original image of Tiexian Jiao, the Hedley method, the Goodman method, and the ND-SGC method, respectively. (I–L) are the original image of Taiping Island, the Hedley method, the Goodman method, and the ND-SGC method, respectively.

3.2. Spectral Fidelity Analysis

Excessive variation of the spectra may lead to spectral distortion and affect the accuracy of bathymetric inversion. Here, we use three indexes, namely; correlation coefficient, error and spectral angle, to measure the spectral correlation; spectral deviation and spectral angle distortion of satellite images before and after sun glint correction.

Figure 4 shows the spectral fidelity index values of the three sun glint correction methods. The CC index values of ND-SGC method, Hedley's method, and Goodman's method were in the range of 0.87–0.91, 0.05–0.46, and 0.20–0.42 in the three study areas, respectively. Hedley's and Goodman's spectral correlation coefficients for satellite images in all three regions were below 0.5. The spectral correlation coefficient is too low, indicating that the Hedley method and the Goodman method make the spectral difference between the sun glint-corrected image and the original image too large, and the inherent information of the image needed for bathymetric inversion may therefore be lost. The Error index values of the ND-SGC method, Hedley's method, and Goodman's method were in the range of 0.02–0.03, 0.05–0.86, and 0.03–0.08, respectively, and the SAM index values were in the range of 0.10–0.55, 0.69–1.53, and 0.64–1.42, respectively. The ND-SGC method has the largest spectral correlation coefficients in all three regions, while the deviation and

spectral angle are both minimal. That is, the ND-SGC method best preserves the inherent information of the image.

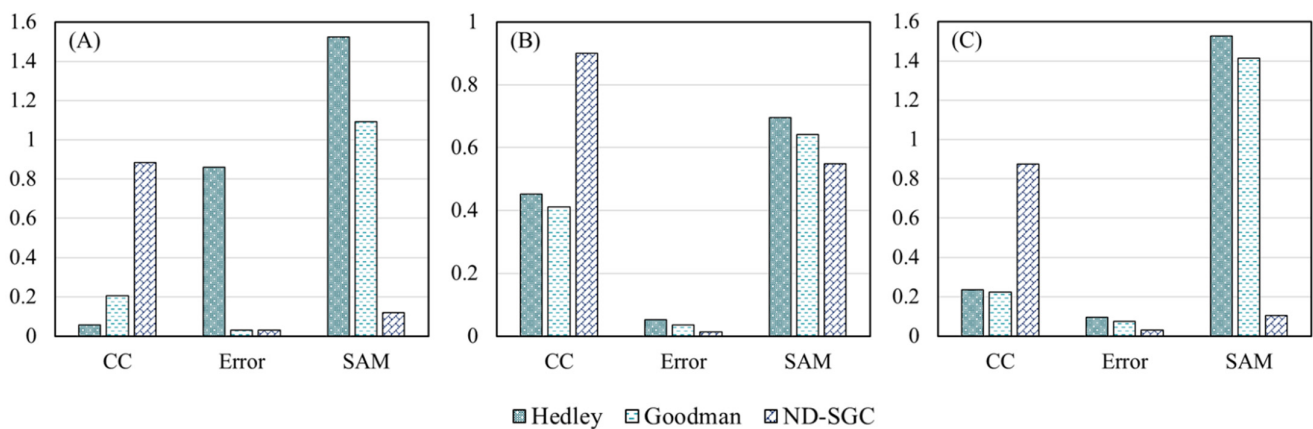


Figure 4. Spectral fidelity evaluation indexes of three sun glint correction methods for three study areas. (A) Dongdao Island; (B) Tiexian Jiao; (C) Taiping Island.

The sun glint correction performed by the ND-SGC method on the satellite images did not cause any spectral distortion of the images. However, the spectral fidelity indexes of the image corrected with the traditional glint correction methods show that the image spectrum has a certain degree of distortion, which will generally have a negative impact on the bathymetric inversion.

Sun glint correction may result in negative values in some bands of some image pixels of satellite images. Negative-valued bands cannot participate in the bathymetric inversion of the corresponding image pixels, which reduces the number of bands participating in the model and usually decreases the accuracy of the bathymetric inversion. Taking the red band, which is most prone to negative values, as shown in Figure 5, the ND-SGC method has only a few negative values or even no negative values in the three study areas, while the conventional method has very many negative image pixels in the red band, and the Hedley method has significantly more negative image pixels in the red band than the Goodman method. Since the reflectance of the reef disk is higher than that outside the reef disk, the change of reflectance of image pixels in the reef disk area is lower than that outside the reef disk under the same degree of sun glint correction, so the negative red band image pixels of the three remote sensing images are mainly concentrated outside the reef disk. The red band binary images of the Hedley and Goodman methods in Dongdao Island are very close to each other. This is probably due to the fact that the near-infrared band values are absorbed by water to a greater extent in the deeper Dongdao Island region than in the remaining two regions, so the overcorrection phenomenon of the two traditional sun glint correction methods is not as serious as in the remaining two regions.

3.3. Effect of Sun Glint Correction on Bathymetric Inversion Results in Different Water Depth Ranges

In this paper, four scenarios are classified according to different water depth ranges: extremely shallow water, shallow water 2–11 m, shallow water 11–20 m and multi-depth range conditions. The water depth data of Taiping Island area ranges from 0–2 m, which belongs to extremely shallow water condition. The range of bathymetry data for Tiexian Jiao is 4 to 11 m. This bathymetry range does not include the extremely shallow water range that is susceptible to distortion by the substrate and the relatively deep water range that is susceptible to water quality. This bathymetry range deserves separate study. The relatively deep shallow water 11–20 m was studied with the Dongdao Island as the study area. The bathymetry data in the Dongdao Island area ranges from 2 to 20 m, which is the most common bathymetry inversion range and contains a variety of bathymetry scenarios

and is a multi-depth section shape. Using the Log-Linear model and Stumpf model as the water depth inversion model. Both models require true bathymetric training points to fit the inversion model parameters, and true bathymetric validation points to rate the bathymetric inversion accuracy. The spatial distribution of true water depth training points and validation points is shown in Figure 1.

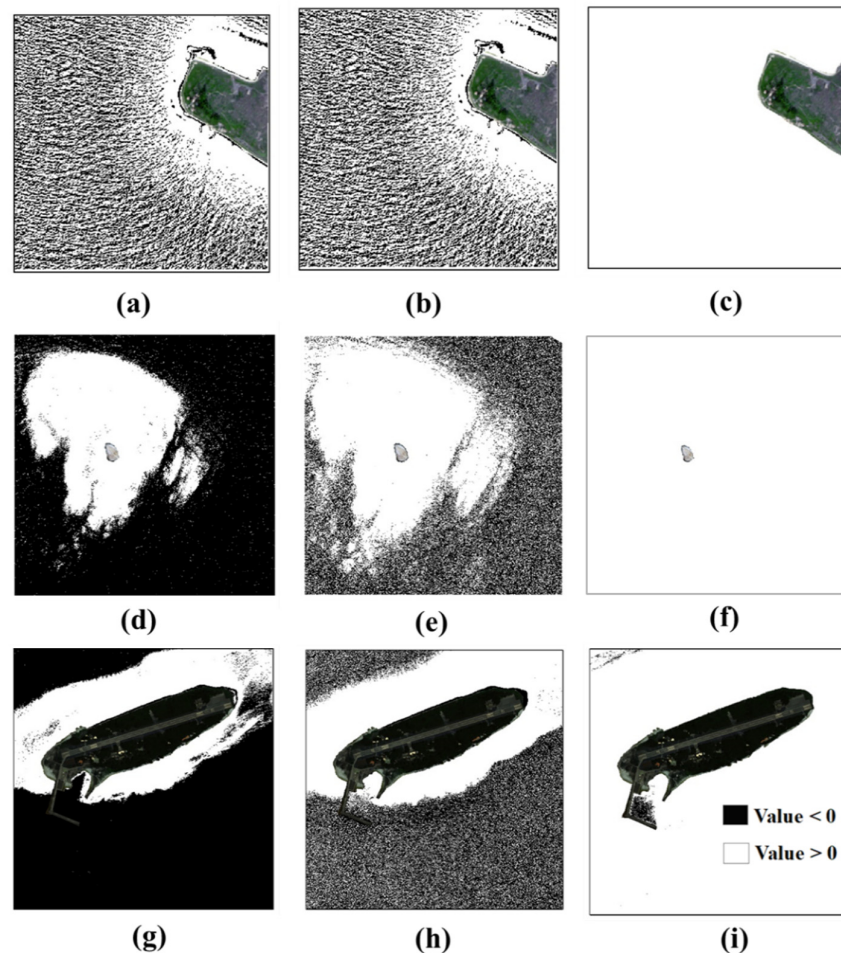


Figure 5. Red band binary images of Dongdao Island, Tiexian Jiao and Taiping Island after sun glint correction. (a–c) Hedley’s method, Goodman’s method and ND-SGC method in Dongdao Island, respectively; (d–f) Hedley’s method, Goodman’s method and ND-SGC method in Tiexian Jiao, respectively; (g–i) Hedley’s method, Goodman’s method and ND-SGC method in Taiping Island, respectively.

3.3.1. Extremely Shallow Water Condition

In this paper, Taiping Island was used as the study area under the extremely shallow water condition. The evaluation of the accuracy of the bathymetric inversion in this region is shown in Figure 6A. The MRE of the Log-Linear and Stumpf models before sun glint correction was 12.5% and 13.2%, respectively. The traditional methods have all reduced the accuracy of bathymetric inversion to different degrees. The Hedley method increased the MRE of the Log-Linear and Stumpf models by 0.6% and 1.4%, respectively. The Goodman’s method increased the MRE of the Log-Linear and Stumpf models by 1.2% and 0.1%, respectively. The ND-SGC method maintained the accuracy of bathymetric inversion in extremely shallow water areas. During the water depth inversion, the extremely shallow water depth was not only easily affected by the substrate, but also the NIR was not completely absorbed by the water body. Therefore, the conventional sun glint correction methods, which are based on the premise that the reflectance in the NIR band is approximately zero, was

not applicable in this water depth range and would have reduced the accuracy of the bathymetric inversion.

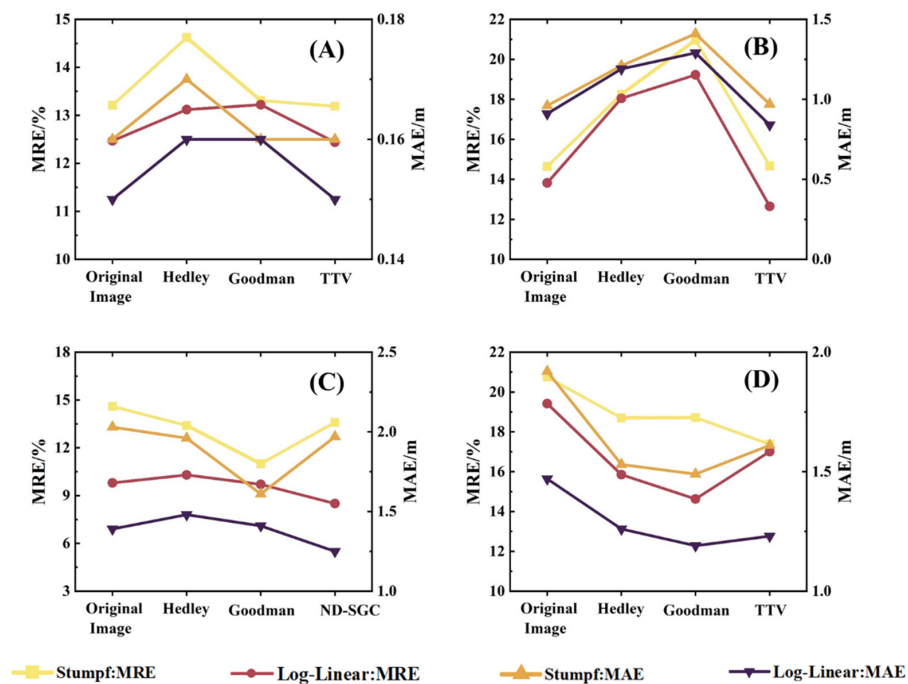


Figure 6. Water depth inversion accuracy of uncorrected images and images corrected by three sun glint correction models. (A) Taiping Island; (B) Tiexian Jiao; (C) Dongdao Island (11–20 m); (D) Dongdao Island (2–20 m).

3.3.2. Shallow Water 2–11 m

Figure 6B shows the accuracy of two bathymetric inversion models for the Tiexian Jiao in shallow water from 4 to 11 m depth. Before sun glint correction, the MREs of the Log-Linear and Stumpf models were 13.8% and 14.6%, respectively. As can be seen in Figure 6B, the ND-SGC method increased the bathymetric inversion accuracy, indicating that the model can be applied to this water depth range. Hedley's method and Goodman's method increased the MRE of the Log-Linear model by 4.3% and 5.4% and the MAE by 0.28 m and 0.38 m, respectively; and increased the MRE of Stumpf by 3.6% and 6.3% and the MAE by 0.25 m and 0.45 m. In the case of shallow water 2–11 m depth, the traditional model reduced the accuracy of water depth inversion. This may be due to the influence of the substrate, where the precondition of non-zero reflectance in the NIR band did not hold, leading to overcorrection in the two conventional models.

3.3.3. Shallow Water 11–20 m

Shallow water 11–20 m is the depth range where the accuracy of optical bathymetry inversion is high. The inversion accuracy of the two water depth inversion models in Dongdao Island is shown in Figure 6C. In this water depth section, the ND-SGC method made the MRE of the two water depth inversion models lower than 14%, and also reduced the MAE of the two water depth inversion models. Although the two traditional models reduced the MRE and MAE of the Stumpf model, they increased the MRE or MAE of the Log-Linear model. This shows that the traditional model is unstable.

3.3.4. Multi-Depth Range Condition

The accuracy of the inversion results of the two bathymetric inversion models for Dongdao Island is shown in Figure 6D. Before the sun glint correction, the MREs of the Log-Linear and Stumpf models were 19.4% and 20.8%, respectively. After sun glint correction, the Log-Linear

model had a maximum reduction of 4.8% in MRE and 0.28 m in MAE. Stumpf's MRE was reduced by a maximum of 3.4% and MAE by a maximum of 0.43 m. In the multi-depth range condition, the ND-SGC method did not differ significantly from the conventional method for bathymetric inversion. In this water depth case, the water was deep enough to fully absorb the NIR. Moreover, the sediment did not affect the water depth inversion model, so the conventional models also improved the accuracy of the bathymetry inversion.

3.4. Effect of Sun Glint Correction on Water Depth Inversion of Pixels with Sun Glint and without Sun Glint

The sun's rays are mirrored directly into the remote sensor, forming sun glint on some of the image pixels of the remote sensor, which are called sun glint pixels, and can be seen as the red boxes in Figure 7a–c. The image pixels that are not contaminated by sun glint are called sun glint-free pixels, see the blue boxes in Figure 7a–c. In general, the reflectance of sun glint pixels contains less effective information than that of sun glint-free pixels, which may make the water depth inversion of sun glint pixels less effective than that of sun glint-free pixels. The effects of different sun glint correction methods on the depth inversion accuracy of sun glint pixels and sun glint-free pixels have been compared.

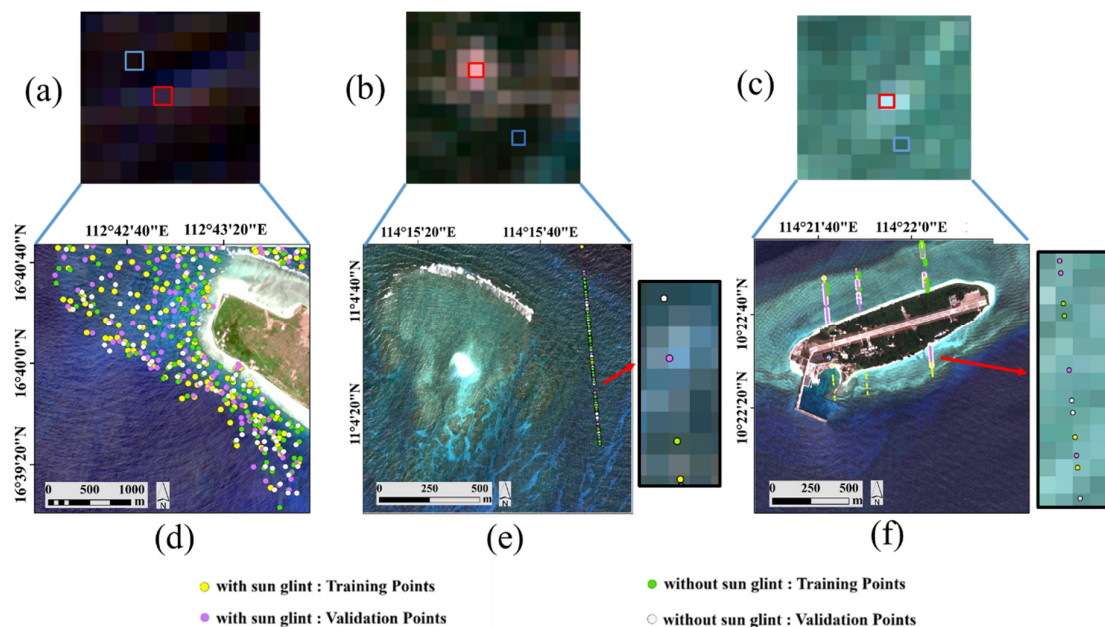


Figure 7. Schematic diagram of sun glint and sun glint-free pixels and spatial distribution of bathymetric training points and validation points in the three study areas. The red box represents the sun glint pixels, the blue box represents the sun glint-free pixels. (a) Schematic diagram of the sun glint and sun glint-free pixels of the Dongdao Island; (b) Schematic diagram of the sun glint and sun glint-free pixels of the Tiexian Jiao; (c) Schematic diagram of the sun glint and sun glint-free pixels of the Taiping Island; (d) Spatial distribution of bathymetric training points and validation points of sun glint and sun glint-free pixels in Dongdao Island; (e) Spatial distribution of bathymetric training points and validation points of sun glint and sun glint-free pixels in Tiexian Jiao; (f) Spatial distribution of bathymetric training points and validation points of sun glint and sun glint-free pixels in Taiping Island.

As can be seen in Figure 8, before the sun glint correction, the dispersion degree of bathymetry points on the glint pixels of Dongdao Island was greater than that on the glint-free pixels, and the inversion accuracy of both bathymetry models on the glint pixels was lower than that on the glint-free pixels. Among them, the MRE of the Log-Linear model of the sun glint pixels was 4.5% higher than that of the sun glint-free pixels and the MAE was 0.20 m higher. The MRE of Stumpf of the sun glint pixels was 1.7% higher and

the MAE was 0.08 m higher than that of the sun glint-free pixels. After the correction of the three sun glint correction methods, the dispersion degree of the bathymetric scatter plot of sun glint pixels and sun glint-free pixels was greatly reduced, and the accuracy of the bathymetric inversion was improved to different degrees. Sun glint correction reduced the MRE of the Log-Linear model of the sun glint pixels from 21.9% to 12.9% maximum, and the MAE from 1.55 m to 1.08 m maximum. Similarly, the MRE of the Stumpf model was reduced from 20.3% to 15.7% at maximum and the MAE was reduced from 1.78 m to 1.26 m at maximum. The MRE of the Log-Linear model with sun glint-free pixels was reduced from 17.4% to 14.5% maximum, and the MAE was reduced from 1.35 m to 1.13 m maximum; the MRE of the Stumpf model was reduced from 18.6% to 15.3% maximum, and the MAE was reduced from 1.70 m to 1.38 m maximum. The improvement of the water depth inversion accuracy of the sun glint pixels was greater than that of the sun glint-free pixels.

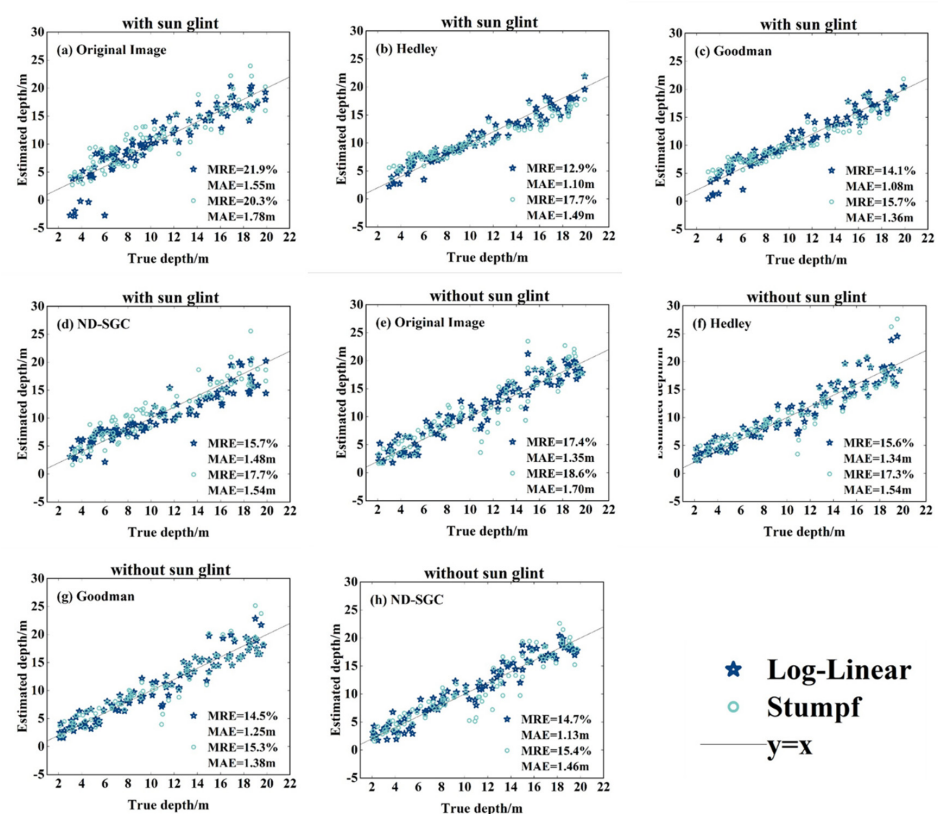


Figure 8. Bathymetric scatter plots of two bathymetric inversion models of the sun glint pixels and sun glint-free pixels of Dongdao Island, and the MRE and MAE of bathymetric inversion. (a) Sun glint pixels of the original image; (b) Sun glint pixels after Hedley's method correction; (c) Sun glint pixels after Goodman's method correction; (d) Sun glint pixels after ND-SGC method correction. (e) Sun glint-free pixels of the original image; (f) Sun glint-free pixels after Hedley's method correction. (g) Sun glint-free pixels after Goodman's method correction; (h) Sun glint-free pixels after ND-SGC method correction.

The indicators for evaluating the accuracy of the bathymetric inversion on sun glint and sun glint-free pixels in Dongdao Island (11–20 m) are shown in Figure 9. Hedley's method increased the MAE and MRE of the Log-Linear model on sun glint pixels and the MAE and MRE of the Stumpf model on glint-free pixels. This indicates the instability of the Hedley method in removing sun glint. As can be seen in Figure 9, Goodman's method and ND-SGC both reduced the MAE and MRE of two bathymetric inversion models. However, the proposed ND-SGC was better than the Goodman method in correcting glint pixels and glint-free pixels.

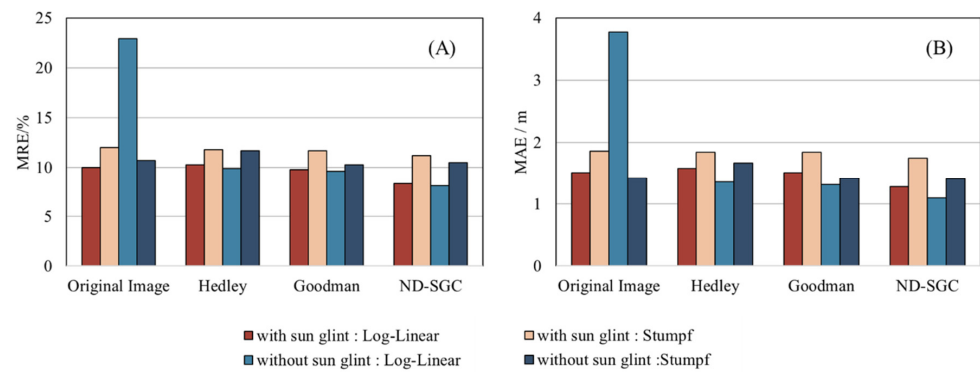


Figure 9. At Dongdao Island (11–20 m), the MRE, MAE of the two bathymetric inversion models on glint pixels and glint-free pixels. (A) MRE; (B) MAE.

Figure 10 shows the evaluation indexes and scatter plots of the bathymetric inversion accuracy on the sun glint pixels and sun glint-free pixels in the Tiexian Jiao. As can be seen in Figure 10, all three sun glint correction models improved the bathymetric inversion accuracy on the sun glint pixels, with the ND-SGC method having the most obvious positive impact on the bathymetric inversion. The ND-SGC method resulted in a maximum reduction of 4.4% in MRE and 0.38 m in MAE for both bathymetric inversion models.

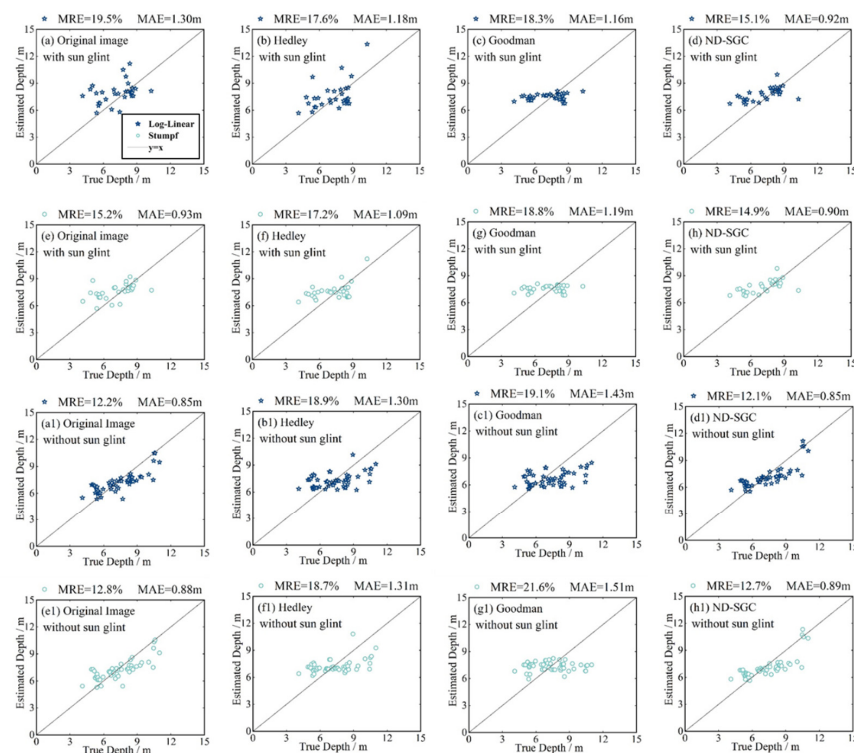


Figure 10. Bathymetric scatter plots of two bathymetric inversion models on the sun glint pixels and sun glint-free pixels of Tiexian Jiao, and the MRE and MAE of bathymetric inversion. (a–d) Log-Linear model bathymetric scatter plots on glint pixels from original image, Hedley’s method, Goodman’s method and ND-SGC method respectively; (e–h) Stumpf model bathymetric scatter plots on glint pixels from original image, Hedley’s method, Goodman’s method and ND-SGC method respectively; (a1–d1) Log-Linear model bathymetric scatter plots on glint-free pixels from original image, Hedley’s method, Goodman’s method and ND-SGC method respectively; (e1–h1) Stumpf model bathymetric scatter plots on glint-free pixels from original image, Hedley’s method, Goodman’s method and ND-SGC method respectively.

As can be seen in Figure 10, the accuracy of water depth inversion before sun glint correction was relatively high, and the MRE of the Log-Linear model and Stumpf model on glint-free pixels was 12.2% and 12.8% respectively. After correction by the ND-SGC method, the MREs of the Log-Linear and Stumpf models on the glint-free pixels were 12.1% and 12.7% respectively, which means that the ND-SGC method maintained the inversion accuracy on the glint-free pixels. The Hedley and Goodman methods resulted in a significant decrease in the accuracy of the bathymetric inversion, with the former increasing the MRE by a maximum of 6.7% and the latter increasing the MRE by a maximum of 8.8%. The scatter plots of Figure 10b,c show a more confusing situation than Figure 10a. These two methods removed the sun glint component equally for all image pixels on the satellite remote sensing image, which tends to overcorrect the sun glint-free pixels and has an impact on the bathymetric inversion. This over-correction phenomenon limits the application of these two traditional methods in shallow water areas.

In the Taiping Island, the ND-SGC method improved or left unchanged the bathymetric inversion accuracy for both types of image pixels (shown in Figure 11) and reduced the MRE by 1.8% and the MAE by 0.01 m at maximum. Thus, this method is still applicable in extremely shallow water areas. Hedley's method and Goodman's method degrade the accuracy of water depth inversion on sun glint pixels and sun glint-free pixels. As shown in Figure 11, the Hedley method increased the MRE by a maximum of 3.4% and the MAE by 0.04 m. The Goodman method increased the MRE by a maximum of 3.4% and the MAE by 0.04 m. The value of NIR is most likely not zero in the extremely shallow water region, which limits the application of the Hedley, Goodman method.

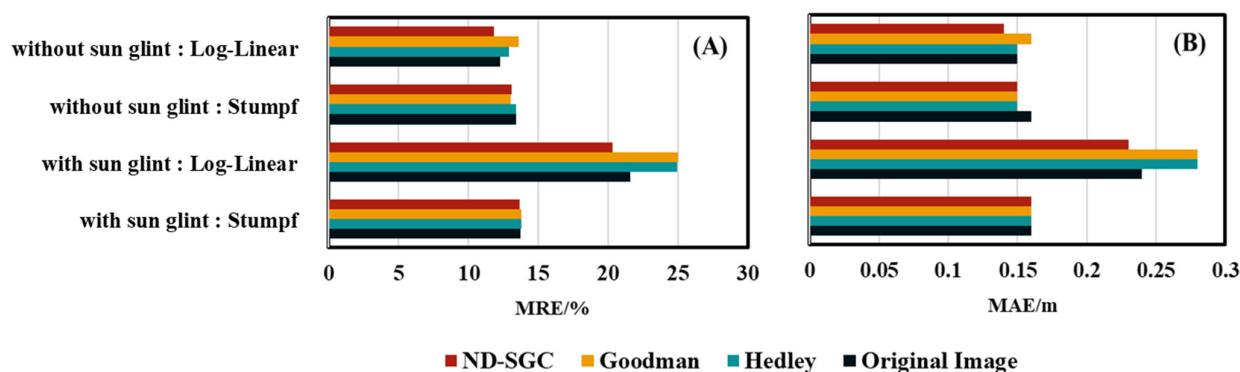


Figure 11. MRE, MAE of two bathymetric inversion models on the sun glint pixels and sun glint-free pixels of Taiping Island. (A) MRE; (B) MAE.

4. Discussion

4.1. The Effect of Spatial Resolution on Glint Correction

The spatial resolution of optical remote sensing images is a major factor on sun glint correction efforts. Sun glints show up differently on remote sensing images of different spatial resolutions. In images with high spatial resolution, the distribution is mostly pepper or thin stripes, while in remote sensing images with low spatial resolution, the distribution is mostly with waves, and the sun glint area is usually larger. Images with different spatial resolutions provide different spatial information, which may affect the sun glint correction.

The accuracy of water depth inversion results is an important way to show the effect of sun glint correction. In WorldView-2 remote sensing images, the ND-SGC method improved the accuracy of water depth inversion in the extremely shallow water range and shallow water range of 2–11 m. To estimate whether the advantage of extremely shallow water range and special shallow water range of ND-SGC method exists on Sentinel-2 remote sensing images, we performed bathymetric inversion of the 2–10 m water depth ranges on Sentinel-2 remote sensing images of Dongdao Island.

The evaluation indexes of bathymetric inversion accuracy for different water depth ranges of Sentinel-2 remote sensing images are shown in Table 3. Table 3 shows that the ND-SGC method still increased the bathymetric inversion accuracy in the very shallow water depth range and the shallow water range from 2 to 10 m. In particular, it significantly increased the bathymetric inversion accuracy of the Log-Linear model. This proves that the ND-SGC method is still applicable in the 2–10 m water depth ranges. In the extremely shallow water range, the ND-SGC method improved the bathymetric inversion accuracy on sun glint pixels more than that on sun glint-free pixels, which is consistent with its performance in WorldView-2 remote sensing images. The Hedley and Goodman methods significantly reduced the inversion accuracy on the sun glint pixels and sun glint-free pixels in this water depth range. In shallow water from 2 to 10 m, the three sun glint correction models have little effect on the accuracy of the water depth inversion on the sun glint pixels. However, the ND-SGC method increased or maintains the accuracy of bathymetric inversion on sun glint-free pixels, while the two conventional methods negatively affect the bathymetric inversion on sun glint-free pixels.

Table 3. Evaluation of the accuracy of water depth inversion of the extremely shallow water and shallow water 2–10 m of the Sentinel-2 image in the Dongdao Island region.

Accuracy	Method	Pixels of All Types		With Sun Glint		Without Sun Glint	
		Log-Linear	Stumpf	Log-Linear	Stumpf	Log-Linear	Stumpf
0–2 m: MRE/%	Original Image	40.0	64.5	55	79.5	41.1	43
	Hedley	59.3	65.2	77.2	80.4	43.5	44.2
	Goodman	57.9	65.8	93.4	80.0	42.5	43.7
	ND-SGC	38.0	61.9	30.5	76.2	38.9	41.4
2–10 m: MRE/%	Original Image	13.1	20.1	16.0	23.6	17.6	19.9
	Hedley	14.4	17.4	16.1	23	17.8	27.7
	Goodman	13.6	16.0	15.7	21.4	17.7	17.9
	ND-SGC	11.8	18.7	14.4	22.3	15.4	19.2
0–2 m: MAE/m	Original Image	0.36	0.48	0.39	0.52	0.40	0.41
	Hedley	0.46	0.49	0.50	0.53	0.41	0.41
	Goodman	0.45	0.49	0.49	0.53	0.42	0.41
	ND-SGC	0.36	0.47	0.36	0.49	0.40	0.42
2–10 m: MAE/m	Original Image	0.84	1.23	0.98	1.38	0.91	1.63
	Hedley	0.94	1.09	1.01	1.31	0.94	1.96
	Goodman	0.89	1.01	0.98	1.25	0.92	0.92
	ND-SGC	0.76	1.18	0.88	1.33	0.81	0.99

4.2. Parameter Settings

The parameter μ and the parameter η are two important parameters of the ND-SGC method. It is necessary to analyze the values of these two parameters. The parameter analysis was carried out on the images of three areas with error as the evaluation indicator for the performance of the parameters. In the experiments, the parameter μ was set in steps of 0.5 from 1 to 3 and the parameter η was set in steps of 0.005 from 0.01 to 0.025. As can be seen in Figure 12, the error values were lower for all three remote sensing images when the parameter μ was equal to 2 and the parameter η was equal to 0.015. When taking other values for parameters, the error can only be low on one or two images. Therefore, the parameters μ and η which are set at 2 and 0.015 respectively can make the ND-SGC perform better.

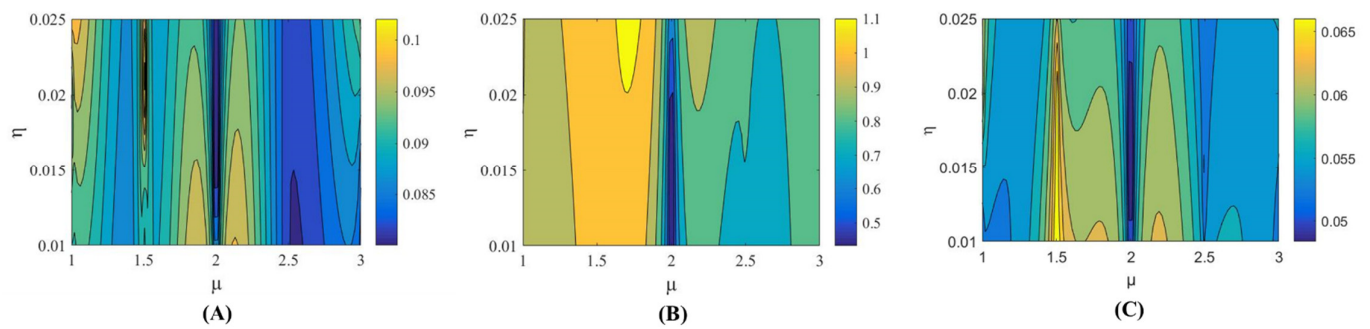


Figure 12. Contour map of Error relative to μ and η . (A) Taiping Island; (B) Tiexian Jiao; (C) Dongdao Island.

4.3. Repetitive Experiments

Uncertainty of ground truth bathymetry data may affect the accuracy of bathymetric inversions. It is necessary to select a new set of field bathymetry data to repeat the experiment. Figure 13 shows the comparison of water depth inversion accuracy of the Stumpf model and the Log-Linear model between the images corrected by three glint correction methods and the original image under four different water depths. It can be seen from Figure 13 that in the four water depth cases, Hedley's method and Goodman's method both caused the accuracy of water depth inversion to become worse, which is most obvious in the Tiexian Jiao and the Dongdao Island (2–20 m). The water depth inversion accuracy on the glint-free pixels corrected by traditional models decreased more than that on the glint pixels. Traditional models are prone to overcorrection. The ND-SGC method did not reduce the accuracy of water depth inversion. In addition, the ND-SGC method reduced the MRE of Taiping Island (0–2 m) by 1.6%, the MRE of Tiexian Jiao (4–11 m) by 3.9%, the MRE of Dongdao Island (11–20 m) by 4.5%, and the MRE of Dongdao Island (2–20 m) by 6.3%. The ND-SGC method still performed well in repeated experiments with a new set of ground truth bathymetry data.

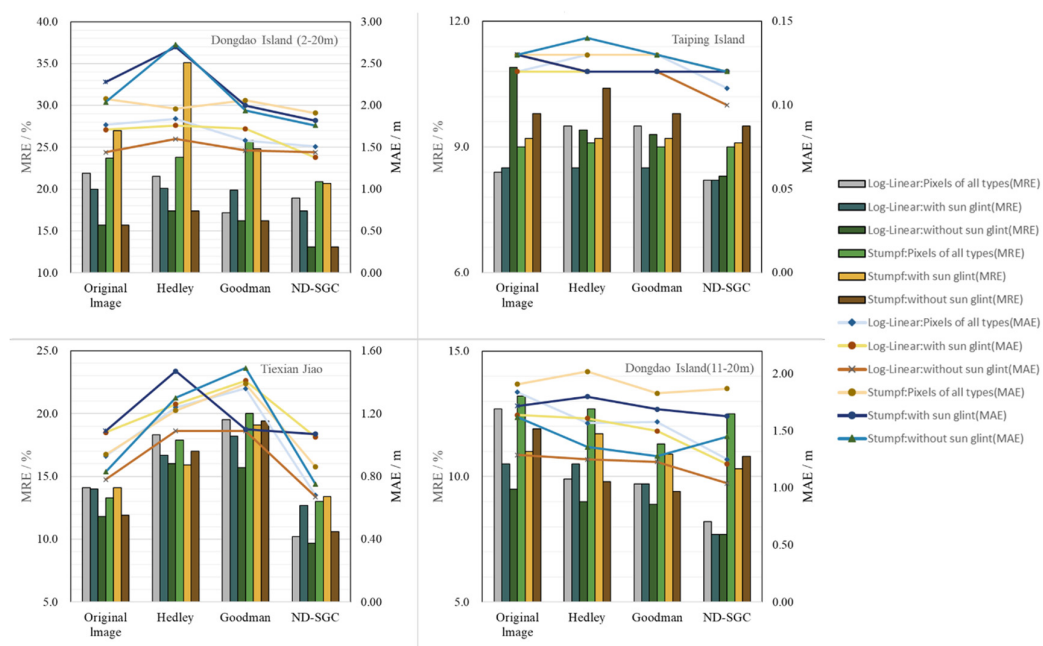


Figure 13. Water depth inversion accuracy of all types of pixels, glint pixels and glint-free pixels before and after sun glint correction. The bar chart represents MRE, and the line chart represents MAE.

Spatial differences may also lead to different sun glint correction methods. Similarly, the temporal difference in the same space is also a major factor in sun glint correction. A Sentinel-2 image of the Dongdao Island, imaged on 19 February 2020, was used to compare different images in the same space. Figure 14 shows the results after correction by several sun glint correction methods. The Hedley and the Goodman method made a particular band stand out and visual aberrations to occur. As shown in the yellow box in Figure 14, the ND-SGC method removed the sun glint noise attached to the waves, and did not cause significant visual distortion in the remote sensing image.

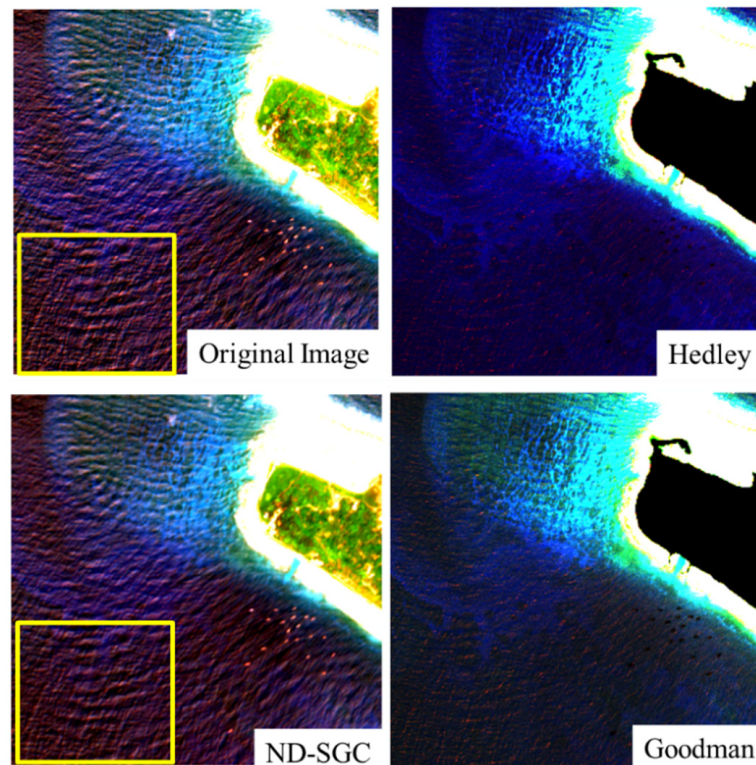


Figure 14. Results of different sun glint correction methods.

Table 4 shows the inversion accuracy of water depth of Log-Linear before and after sun glint correction. In water depths of 4–11 m, each sun glint correction method improved the bathymetric inversion accuracy on glint pixels, while the conventional methods degraded the bathymetric inversion accuracy on glint-free pixels. In water depths of 11–20 m, the ND-SGC method improved the accuracy of the bathymetric inversion more than the traditional methods. The ND-SGC method reduced the MRE by a maximum of 5.5% and the MAE by a maximum of 0.89 m over this water depth range. In water depths of 2 to 20 m, the two traditional methods reduced the accuracy of the bathymetric inversion on glint-free pixels. The Hedley's method, the Goodman's method and the ND-SGC methods reduced the MRE of the glint pixels by 3.7%, 4.8% and 7.8%, respectively. The ND-SGC method was more effective than the two conventional models in the multi-depth section scenario of 2 to 20 m.

Table 5 shows the water depth inversion accuracy of the Stumpf model. In each water depth section, the three sun glint correction models have improved the accuracy of water depth inversion. The ND-SGC method had a greater effect on the accuracy of the bathymetric inversion of the Stumpf model than the other two models. In the water depth of 2–11 m, the ND-SGC method reduced the MRE on sun glint pixels by 7.8% and that on glint-free pixels by 7.2%. The ND-SGC method also showed advantages over the other two methods in the water depths of 11–20 m and 2–20 m.

Table 4. Evaluation of bathymetric inversion accuracy of the Log-Linear model for Sentinel-2 image of Dongdao Island on 19 February 2020.

		Pixels of All Types		With Sun Glint		Without Sun Glint	
	Method	MRE/%	MAE/m	MRE/%	MAE/m	MRE/%	MAE/m
2–11 m	Original Image	22.1	1.60	39.4	2.12	33.1	1.83
	Hedley	27.4	1.91	32.0	1.89	40.5	2.02
	Goodman	23.4	1.63	28.2	1.72	34.3	1.76
	ND-SGC	21.9	1.60	26.9	1.58	30.8	1.67
11–20 m	Original Image	14.9	2.38	12.7	1.95	11.6	1.85
	Hedley	14.1	2.26	11.8	1.80	13.4	2.14
	Goodman	15.2	2.45	12.9	1.98	14.1	2.25
	ND-SGC	9.4	1.49	8.7	1.24	9.9	1.58
2–20 m	Original Image	21.5	2.10	24.5	1.99	22.2	1.81
	Hedley	21.5	2.11	20.8	1.82	26.8	2.09
	Goodman	20.1	2.08	19.7	1.86	24.1	2.02
	ND-SGC	19.6	1.67	16.7	1.36	20.2	1.61

Table 5. Evaluation of bathymetric inversion accuracy of the Stumpf model for Sentinel-2 image of Dongdao Island on 19 February 2020.

		Pixels of All Types		With Sun Glint		Without Sun Glint	
	Method	MRE/%	MAE/m	MRE/%	MAE/m	MRE/%	MAE/m
2–11 m	Original Image	28.2	2.6	32.8	2.68	28.7	2.57
	Hedley	24.1	2.3	29.4	2.50	25.9	2.36
	Goodman	22.1	2.15	28.1	2.36	23.6	2.18
	ND-SGC	21.9	2.13	25.0	2.15	21.5	2.00
11–20 m	Original Image	31.0	2.37	37.0	2.63	29.9	2.48
	Hedley	26.0	2.06	32.8	2.68	26.8	2.28
	Goodman	23.2	1.96	31.4	2.28	24.2	2.09
	ND-SGC	23.1	1.84	28.0	2.12	22.6	1.97
2–20 m	Original Image	28.1	2.60	32.6	2.63	28.4	2.57
	Hedley	24.0	2.30	29.2	2.45	25.6	2.36
	Goodman	22.0	2.15	27.9	2.33	23.3	2.18
	ND-SGC	21.8	2.13	24.9	2.12	21.2	1.99

5. Conclusions

Unlike the conventional methods that are limited by the water depth range, the noise de-correlation-based sun glint correction method proposed in this paper is applicable to different water depth ranges. In the range of extremely shallow water and special shallow water range 2–10 m, the model showed advantages and improved the accuracy of water depth inversion in the above two special areas.

The ND-SGC method retained intrinsic spectral information useful for bathymetric inversion of remote sensing images while removing sun glint. However, the two traditional sun glint correction methods distorted the remote sensing image spectra to different degrees, and it was very easy to cause negative band values of some image pixels in remote sensing images, which affects the accuracy of water depth inversion.

The method proposed in this paper is based only on the texture structure of the image itself and can be used for images containing only three visible bands, further reducing the reliance on auxiliary information and increasing the types of available remote sensing images. Traditional sun glint correction methods require information from other wavelengths in order to perform sun glint correction in the visible wavelengths, making it difficult to correct images with only red, green and blue wavelengths.

The ND-SGC method has a different intensity of sun glint correction for different image pixels, and the correction intensity for sun glint pixels is higher than that for sun glint-free pixels. On the premise of effectively removing the sun glint component of sun glint pixels, the method avoids the over-correction phenomenon of sun glint-free pixels and maintains the accuracy of water depth inversion of sun glint-free pixels. However, the sun glint correction intensity of the traditional method is the same for both types of image pixels, which tends to make the un-glint-free pixels overcorrected and reduces the accuracy of bathymetry inversion.

Author Contributions: Conceptualization, Y.M. and A.C.; methodology, A.C.; validation, A.C., Y.M., X.Z. and X.Z.; writing—original draft preparation, A.C.; writing—review and editing, Y.M. and J.Z. All authors have read and agreed to the published version of the manuscript.

Funding: National Natural Science Foundation of China (NSFC) [51839002,41906158]; Taishan Scholar Project of Shandong Province [ts20190963]; the China High Resolution Earth Observation System Program [41-Y30F07-9001-20/22].

Data Availability Statement: Sentinel-2 data acquisition website: <https://scihub.copernicus.eu/dhus/#/home>, accessed on 13 February 2021. ICESat-2 data official website: <https://icesat-2.gsfc.nasa.gov/>, accessed on 23 May 2022. The Tide High Data acquisition website: <https://tides4fishing.com/>, accessed on 23 May 2022.

Acknowledgments: Thanks to the Chinese National Programs for High Technology Research and Development (863 Program) that provided the actual water depth data for Dongdao Island and the National Aeronautics and Space Administration (NASA) that provided the ICESat-2 data for Tiexian Jiao and Taiping Island. Furthermore, we gratefully acknowledge the European Space Agency (ESA) for providing the Sentinel-2 productions.

Conflicts of Interest: The authors declare no conflict of interest.

References

1. Ashpbaq, M.; Srivastava, P.K.; Mitra, D. Review of near-shore satellite-derived bathymetry: Classification and account of five decades of coastal bathymetry research. *J. Ocean Eng. Sci.* **2021**, *6*, 340–359. [CrossRef]
2. Geyman, E.C.; Maloof, A.C. A simple method for extracting water depth from multispectral satellite imagery in regions of variable bottom type. *Earth Space Sci.* **2019**, *6*, 527–537. [CrossRef]
3. Sagawa, T.; Yamashita, Y.; Okumura, T.; Yamanokuchi, T. Satellite derived bathymetry using machine learning and multi-temporal satellite images. *Remote Sens.* **2019**, *11*, 1155. [CrossRef]
4. Hedley, J.D.; Roelfsema, C.; Brando, V.; Giardino, C.; Kuster, T.; Phinn, S.; Mumby, P.J.; Barrilero, O.; Laporte, J.; Koetz, B. Coral reef applications of Sentinel-2: Coverage, characteristics, bathymetry and benthic mapping with comparison to Landsat 8. *Remote Sens. Environ.* **2018**, *216*, 598–614. [CrossRef]
5. Olayinka, I.C.; Knudby, A. Satellite-derived bathymetry using a radiative transfer-based method: A comparison of different atmospheric correction methods. In Proceedings of the OCEANS 2019 MTS/IEEE SEATTLE, Seattle, WA, USA, 27–31 October 2019.
6. Lyzenga, D.R.; Malinas, N.P.; Tanis, F.J. Multispectral bathymetry using a simple physically based algorithm. *IEEE Trans. Geosci. Remote Sens.* **2006**, *44*, 2251–2259. [CrossRef]
7. Zhang, X.; Ma, Y.; Zhang, J. Shallow water bathymetry based on inherent optical properties using high spatial resolution multispectral imagery. *Remote Sens.* **2020**, *12*, 3027. [CrossRef]
8. Stumpf, R.P.; Holderied, K.; Sinclair, M. Determination of water depth with high-resolution satellite imagery over variable bottom types. *Limnol. Oceanogr.* **2003**, *48*, 547–556. [CrossRef]
9. Ma, Y.; Zhang, J.; Zhang, J.; Zhang, Z.; Wang, J. Progress in Shallow Water Depth Mapping from Optical Remote Sensing. *Adv. Mar. Sci.* **2018**, *36*, 331–351.
10. Zhang, H.; Wang, M. Evaluation of sun glint models using MODIS measurements. *J. Quant. Spectrosc. Radiat. Transf.* **2010**, *111*, 492–506. [CrossRef]
11. Muslim, A.M.; Chong, W.S.; Safuan, C.D.M.; Hossain, M.S. Coral reef mapping of UAV: A comparison of sun glint correction methods. *Remote Sens.* **2019**, *11*, 2422. [CrossRef]
12. Kay, S.; Hedley, J.D.; Lavender, S. Sun Glint Correction of High and Low Spatial Resolution Images of Aquatic Scenes: A Review of Methods for Visible and Near-Infrared Wavelengths. *Remote Sens.* **2009**, *1*, 697–730. [CrossRef]
13. Li, L.; Liu, J.; Zou, B. A method to remove sun glint in depth derivation from World View-2 remote sensing images. *Mar. For.* **2015**, *32*, 53–57.

14. Cox, C.; Munk, W. Measurement of the roughness of the sea surface from photographs of the sun's glitter. *J. Opt. Soc. Am.* **1954**, *44*, 838–850. [\[CrossRef\]](#)
15. Legleiter, C.J.; Mobley, C.D.; Overstreet, B.T. A framework for modeling connections between hydraulics, water surface roughness, and surface reflectance in open channel flows. *Geophys. Res. Earth Surf.* **2017**, *122*, 1715–1741. [\[CrossRef\]](#)
16. Bréon, F.M.; Henriot, N. Spaceborne observations of ocean glint reflectance and modeling of wave slope distributions. *J. Geophys. Res. Ocean.* **2006**, *111*, C06005. [\[CrossRef\]](#)
17. Hochberg, E.J.; Andréfouët, S.; Tyler, M.R. Sea surface correction of high spatial resolution Ikonos images to improve bottom mapping in near-shore environments. *IEEE Trans. Geosci. Remote Sens.* **2003**, *41*, 1724–1729. [\[CrossRef\]](#)
18. Hedley, J.D.; Harborne, A.R.; Mumby, P.J. Simple and robust removal of sun glint for mapping shallow-water benthos. *Int. J. Remote Sens.* **2005**, *26*, 2107–2112. [\[CrossRef\]](#)
19. Goodman, J.A.; Lee, Z.P.; Ustin, S.L. Influence of atmospheric and sea-surface corrections on retrieval of bottom depth and reflectance using a semi-analytical model: A case study in Kaneohe Bay, Hawaii. *Appl. Opt.* **2008**, *47*, F1–F11. [\[CrossRef\]](#)
20. Kutser, T.; Vahtmae, E.; Praks, J. A sun glint correction method for hyperspectral imagery containing areas with non-negligible water leaving NIR signal. *Remote Sens. Environ.* **2009**, *113*, 2267–2274. [\[CrossRef\]](#)
21. Liu, Q.; Liu, J.; Dong, P.; Liang, D. SGTD: Structure gradient and texture decorrelating regularization for image decomposition. In Proceedings of the IEEE International Conference on Computer Vision (ICCV), Sydney, Australia, 1–8 December 2013.
22. He, W.; Zhang, H.; Zhang, L.; Shen, H. Total-variation-regularized low-rank matrix factorization for hyperspectral image restoration. *IEEE Trans. Geosci. Remote Sens.* **2016**, *54*, 178–188. [\[CrossRef\]](#)
23. Zhang, H.; He, W.; Zhang, L.; Shen, H.; Yuan, Q. Hyperspectral image restoration using low-rank matrix recovery. *IEEE Trans. Geosci. Remote Sens.* **2013**, *52*, 4729–4743. [\[CrossRef\]](#)
24. Duan, P.; Lai, J.; Kang, J.; Kang, X.; Ghamisi, P.; Li, S. Texture-aware total variation-based removal of sun glint in hyperspectral images. *ISPRS J. Photogramm. Remote Sens.* **2020**, *166*, 359–372. [\[CrossRef\]](#)
25. Neumann, T.A.; Martino, A.J.; Markus, T.; Bae, S.; Bock, M.R.; Brenner, A.C.; Brunt, K.M.; Cavanaugh, J.; Fernandes, S.T.; Hancock, D.W.; et al. The Ice, Cloud, and Land Elevation Satellite -2 mission: A global geolocated photon product derived from the Advanced Topographic Laser Altimeter System. *Remote Sens. Environ.* **2019**, *233*, 111325. [\[CrossRef\]](#)
26. Ma, Y.; Xu, N.; Liu, Z.; Yang, B.; Yang, F.; Wang, X.H.; Li, S. Satellite-derived bathymetry using the ICESat-2 Lidar and Sentinel-2 imagery datasets. *Remote Sens. Environ.* **2020**, *250*, 112047. [\[CrossRef\]](#)
27. Meyer, Y. *Oscillating Patterns in Image Processing and Nonlinear Evolution Equations*; American Mathematical Society: Providence, RI, USA, 2001; pp. 22–23.
28. Chen, T.; Yin, W.; Zhou, X.; Comaniciu, D.; Huang, T. Total variation models for variable lighting face recognition. *IEEE Trans. Pattern. Anal. Mac. Int.* **2006**, *28*, 1519–1524. [\[CrossRef\]](#) [\[PubMed\]](#)
29. Li, X.; Lu, C.; Xu, Y.; Jia, J. Image smoothing via 0 gradient minimization. *ACM Trans. Graphics* **2011**, *30*, 174.
30. Li, X.; Yan, Q.; Yang, X.; Jia, J. Structure extraction from texture via relative total variation. *ACM Trans. Graphics* **2012**, *31*, 139.